Design of an Anthropomorphic, Compliant, and Lightweight Dual Arm for Aerial Manipulation

ALEJANDRO SUAREZ, GUILLERMO HEREDIA, AND ANIBAL OLLERO

Robotics, Vision and Control Group, University of Seville, 41092 Seville, Spain

Corresponding author: Guillermo Heredia (guiller@us.es)

ABSTRACT This paper presents an anthropomorphic, compliant and lightweight dual arm manipulator designed and developed for aerial manipulation applications with multi-rotor platforms. Each arm provides four degrees of freedom in a human-like kinematic configuration for end effector positioning: shoulder pitch, roll and yaw, and elbow pitch. The dual arm, weighting 1.3 kg in total, employs smart servo actuators and a customized and carefully designed aluminum frame structure manufactured by laser cut. The proposed design reduces the manufacturing cost as no computer numerical control machined part is used. Mechanical joint compliance is provided in all the joints, introducing a compact spring-lever transmission mechanism between the servo shaft and the links, integrating a potentiometer for measuring the deflection of the joints. The servo actuators are partially or fully isolated against impacts and overloads thanks to the flange bearings attached to the frame structure that support the rotation of the links and the deflection of the joints. This simple mechanism increases the robustness of the arms and safety in the physical interactions between the aerial robot and the environment. The developed manipulator has been validated through different experiments in fixed base test-bench and in outdoor flight tests.

INDEX TERMS Aerial manipulation, aerial robots, design of floating-base manipulators, compliance.

I. INTRODUCTION

Aerial manipulation proposes the development of flying robots equipped with one or more [1] robotic arms capable to perform certain operations in workspaces out of the reach for humans. This technology is intended to simplify and reduce the costs associated to inspection and maintenance tasks that are typical in a wide variety of scenarios in the industry. Some examples include the detection and repair of leaks in high altitude pipes in chemical plants, the insulation of cracks in the blades in wind turbines, the installation and retrieval of sensor devices in buildings and other structures, or the measurement of the deflection in the metal beams in bridges.

The platforms employed in aerial manipulation are vertical take-off and landing (VTOL) unmanned aerial vehicles (UAV) due to the necessity of staying in hover during the execution of the operation carried out by the robotic arms. Autonomous helicopters [2], [3] and quadrotors [4] have been employed in grasping and transportation tasks in outdoors. Grasping moving objects [5] and cooperative grasping with multiple UAVs [6] have been also

demonstrated previously. Two approaches can be identified in the development of aerial manipulation robots: 1) integrating a conventional robotic arm designed for ground applications, or 2), designing a specific manipulator intended to aerial platform. The first approach is followed in [2] and [7], where a 7 degrees of freedom (DOF's) industrial manipulator is integrated in a helicopter with high payload capacity, or in [4], where a quadrotor is equipped with a 7-DOF robotic arm commercially available. Several research prototypes have been designed for multirotors and tested on flight, with different number of degrees of freedom, from two up to seven [8]–[12]. Aerial manipulators have been applied in a wide variety of applications, including valve turning with quadrotors [13], visual servoing [14], contact based inspection [15], or grasping [16], [17].

Mechanical compliance is a highly desirable feature for an aerial manipulation robot as it increases safety in operations involving physical interactions with the environment [18]–[20]. The ability of springs and other elastic elements for absorbing the energy of impacts and overloads at

higher rates than the actuators can provide in a passive way prevents that contact forces are rigidly propagated through the manipulator to the aerial platform, destabilizing it. Series elastic actuators [21] introduce an elastic transmission element between the actuator and the output link, allowing the estimation of the forces based on deflection measurement. This principle can be exploited in low weight robotic arms built with low cost servos that do not provide any torque control or feedback capabilities. That is, the joint torque and the contact forces can be estimated just measuring the deflection of the elastic element [22]–[24]. Mechanical joint compliance also protects the gearbox of the servos against peak forces caused by impacts, the transition from contactless to contact situations, or overloads caused by motion constraints, for example in closed kinematic chain configurations. In our previous work, two research prototypes of human-size, compliant and very low weight robotic arms where developed, demonstrating their application to soft collision detection and reaction, payload estimation [25], force torque estimation and control, and obstacle localization [26].

TABLE 1. Main features of different aerial manipulators.

Ref	Stiff / Compliant	Single / Dual	Num. joints	Reach [m]	Weight/Lift load [kg]
Proposed	Compliant	Dual	8	0.5	1.3 / 0.2
[26]	Compliant	Single	3	0.5	0.3 / 0.2
[20]	Compliant	Single	1	0.18	0.36 / NA
[28]	Stiff	Dual	10	0.5	1.8 / 0.75
[13]	Stiff	Dual	4	NA	NA / NA
[11]	Stiff	Single	6	0.45	1.4 / NA
[10]	Stiff	Single	5	0.3	0.25 / 0.2

Bimanual manipulation has been considered in some recent works, as the valve turning task described in [13], the grasping and transportation application shown in [27], or the human-size dual arm aerial manipulator presented in [28]. The main motivation for a dual arm manipulator is to extend the range of tasks that a flying robot is able perform w.r.t. a single arm, allowing for example grasping large objects, manipulating two devices at the same time, or increasing the maximum lift load. This is done however at expenses of increasing the payload of the UAV, so the effort now is in the design of very low weight manipulators [29]. The main features of several lightweight and compliant manipulators are compared in TABLE 1.

The main contribution of the paper is the development and experimental validation of an anthropomorphic, compliant and lightweight (1.3 kg) dual arm manipulator designed for aerial manipulation applications. Each arm provides 4 DOF's for positioning the end effector in a human-like kinematic configuration. A simple and compact compliant transmission mechanism is integrated in all the joints with a deflection potentiometer, allowing the estimation and control of the joint torque and the contact forces. A customized and carefully designed aluminum frame structure manufactured by laser cut isolates the servo actuators against impacts and radial-axial overloads, supporting the rotation of the output links and the

spring-lever transmission. The paper details the design and construction of the arms, covering the kinematics, dynamics, and the force-torque relationships. Identification experiments have been conducted for evaluating the impact response and the frequency behavior. Deflection control experiments show how compliance can be exploited for reducing the interaction forces between the aerial manipulator and the environment on flight. The developed dual arm manipulator was integrated in a hexarotor platform, demonstrating bimanual aerial grasping.

The rest of the paper is organized as follows. Section II introduces some general design considerations related to aerial manipulation. Section III presents the design of the dual arm manipulator with its mechanical specifications, the kinematics and the control architecture. Section IV details the spring-lever transmission mechanism integrated in the joints, deriving the force-torque relationships. Section V describes the structure of the arms, providing the mass and inertia values. Experimental results validating the design are shown in Section VI, whereas Section VII summarizes the conclusions of this work.

II. DESIGN CONSIDERATIONS
A. REQUIREMENTS IN AERIAL MANIPULATION
1) LOW WEIGHT AND INERTIA FEATURES
The first two parameters that should be determined in the design of a robotic arm to be integrated in an aerial platform are its weight and maximum lift load. Let us call PL_{UAV} to the maximum payload that the UAV is able to lift, and m_{arm} and PL_{arm} to the weight and expected payload that the arm should lift, respectively. Then, the following equation can be defined:

$$m_{arm} + PL_{arm} \leq \eta \cdot PL_{UAV} \qquad (1)$$

Here $\eta \cong 0.7$ is the dynamic margin constant that indicates how far away the brushless motors of the UAV are from the saturation in normal operation. If the aerial platform is overloaded ($\eta > 0.8$), the propellers may suffer overheating and they might not respond properly to motion commands.

In order to reduce the inertia of the arms, and thus the influence of arms motion over the aerial platform, it results convenient to place the servos as close as possible to the base of the aerial platform. Different transmission mechanisms can be employed for this purpose, including timing belts [10], pulley-wire [20] or rigid bars [28]. However, these solutions typically increase the weight of the manipulator, reduce the range of rotation of the joints, and complicate the design and assembly of the manipulator.

The mass distribution of the different components employed in the construction of the arms is represented in **Fig. 1**, whereas TABLE 2 indicates the mass density of the materials.

2) ACTUATORS
The design and development of robotic arms intended to aerial manipulation is still a hard task due to the multiple
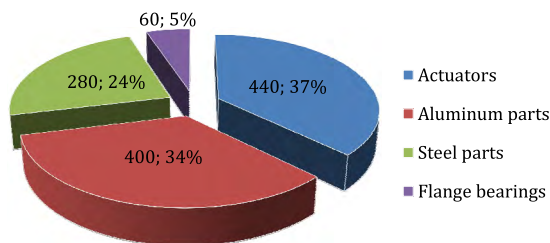
FIGURE 1. Mass distribution (grams and %) of the developed dual arm.

TABLE 2. Materials employed in the lightweight dual arm.

Material	Mass density [g/cm^3]	Description/Application
Aluminium	2.8	Frame structure
Steel	8.75	Screws, nuts, washers and springs
igus® plastic	1.4	EFOM/EFMS flange bearings
Servos	1.5	Equivalent mass density of the actuators

design requirements imposed by the aerial platform in terms of very low weight, low inertia, mechanical robustness and dexterity. What is more, there exist important technological limitations as only a few brands of actuators are suitable for this purpose. In this sense, the so called smart servos, such as Herkulex or Dynamixel, are nowadays the best option for building low weight manipulators [4], [8], [11]. These devices include the motor, gearbox, electronics, control and communications in a compact device that can be easily assembled in a frame structure, providing high torque to weight ratios. However, the performance of these actuators from the control point of view is quite limited, as they do not provide any torque feedback or control, the control rates are usually low (<100 Hz), and the embedded controller has to be interfaced. Although the lift load of the arms should be determined by the application, its value is given in practice by the combination of servo actuators employed, taking into account that the stall torque parameter provided by the manufacturer is usually 2–3 times higher than the maximum dynamic torque that the servo is able to provide.

3) KINEMATICS

The choice of the kinematic configuration of the arms is determined in the first place by the task that the aerial robot is expected to perform. Almost all aerial manipulators that can be found on literature consider at least two joints, shoulder pitch and elbow pitch [8], [9], with the forearm and upper arm links. Some prototypes exploit the rotation of the UAV around the yaw angle instead of employing a servo for this purpose [8]. Other works implement the typical configuration with three joints for positioning and two [10] or three [11] DOF's for wrist orientation. Motivated by the convenience to provide a human-like manipulation capability, this work follows a bio-inspired design approach, so the kinematics and size of the human arm are replicated. The idea is that the application of the arms results more comfortable and intuitive

for a human operator, without requiring special training. The mechanical construction of this configuration also results in a compact and robust design, as it will be seen later.

B. COMPONENTS AND MATERIALS

1) FRAME STRUCTURE

Aluminum and carbon fiber are widely used for building low weight robotic arms intended to aerial manipulation due to their mechanical robustness and low weight. ABS or PLA plastics should be avoided as they are not impact resistant and may suffer deformations for temperatures around 40 ° C. Note that in case of impact, the manipulator will support the kinetic energy of the whole aerial platform (0.625 J for a 5 kg weight platform moving at 0.5 m/s). Most aerial robots employ carbon fiber in the frame structure of the arms. However, the manufacturing cost and the material itself is quite expensive with respect to aluminum. Besides its low cost, aluminum is highly malleable, so L-shaped or U-shaped frames can be easily manufactured bending a flat frame. The possibility of introducing these geometries is important in the design of the frame structure and its parts.

2) COMPLIANT TRANSMISSION

As mentioned before, one of the main contributions of this work is the development of a simple, compact and low weigh spring-lever transmission mechanism integrated in all the joints of the arms to provide compliance. Conventional steel springs are preferred rather than other elastic materials like elastomers due to their high linearity and low hysteresis. The mechanism makes use of igus flange bearings screwed to the aluminum frame structure for supporting the rotation of the output links w.r.t. the servo shafts. These components provide low friction and vibration dampening, being also robust against impacts and radial/axial loads.

FIGURE 2. 3-D model of the anthropomorphic dual arm integrated in a hexarotor. Take-off/landing (left) and operation (right) configurations.

C. INTEGRATION IN AERIAL PLATFORM

In order to maintain the symmetry of the aerial platform in terms of geometry and mass distribution, the manipulator is typically installed under the central hub of the UAV, trying to reduce the displacement of the center of mass (CoM) with respect to the vertical axis. This implies that the arms should be placed between the legs of the landing gear, what may reduce the workspace of the arms due to motion constraints. The solution adopted in this work is the one shown in **Fig. 2**. Thanks to the anthropomorphic kinematic

configuration, the arms can be lifted rotating the shoulder roll joints, so the upper arm and forearm links are above the landing gear for UAV take-off and landing. An adaptation frame consisting of two transversal hollow aluminum profiles is attached to the base of the landing gear. The configuration of the arms during the take-off and manipulation phases can be seen in Section VI-D.

FIGURE 3. Phases involved in the design, development and experimental validation of an aerial manipulation prototype.

D. DEVELOPMENT METHODOLOGY

The development of an aerial manipulation robot involves a number of phases, graphically represented in **Fig. 3**. The first one is the concept design, which consist of defining the main specifications of the manipulator (payload, size, number of joints, capabilities), and drawing different designs on paper to have an idea of its structure. Once a preliminary design is proposed, the different frame parts are modelled using 3D computer aided design software such as CATIA or Solid Edge. It is convenient to specify the mass density of all the components in the model in order to obtain an estimation of the mass and inertia of the prototype during its design. It is also necessary to take into account the limitations and constraints associated to the manufacturing and assembly processes, as stated in Section II-B. Several iterations may be necessary in the design until this can be implemented in the desired way.

Once the prototype is assembled, the next step consists of integrating the sensors, electronics, and wiring in the frame structure. The hardware/software architecture, described in more detail in Section III-C, is the basis for the development of the different functionalities of the aerial manipulator, such as position, trajectory, and force control, collision detection and reaction, teleoperation, or visual servoing for grasping. All these capabilities must be extensively validated in test-bench before integrating the manipulator in the aerial vehicle in order to prevent accidents due to unexpected behaviors, evaluating the reliability and accuracy through experimental results.

The installation of the arms in the multirotor requires an additional frame structure which should be attached at the landing gear or well at the base of the platform. This structure can also support the batteries, the computer board, and other sensors, as the camera. The validation of the aerial robot in outdoor flight tests requires the participation of at least two persons: the pilot of the UAV and the operator of the arms. Security nets and ropes should be used in the first tests for preventing potential crashes, especially if the evaluated task involves contact forces. The position and orientation of the multirotor, the applied control signals, the angular position of the actuators and their references should be logged in data files so the experimental results can be analyzed offline.

FIGURE 4. Anthropomorphic, compliant and lightweight dual arm.

FIGURE 5. Detailed view of the joints in the right arm. Hands-up pose.

III. ANTHROPOMORPHIC DUAL ARM DESIGN

A. DESCRIPTION

A picture of the developed anthropomorphic, compliant and lightweight dual arm manipulator can be seen in **Fig. 4**, with a detailed view of the right arm construction in **Fig. 5**. The dual arm system was designed and developed completely from scratch, although several design concepts are taken from our previous work [25], [26], [28]. The actuators used are the Herkulex DRS-0101 and DRS-0201 smart servos from Dongbu Robot, introducing the igus EFOM-08 and EFSM-06 flange bearings in the frame structure for isolating the servos from impacts and overloads and for building the compliant transmission mechanism. The frame structure of the arms consists of a set of 34 customized aluminum parts manufactured by laser cut, two 8 mm Ø shafts for the shoulder

pitch joint, and four 6 mm Ø hollow profiles for the upper arm and forearm links. The laser cut frames include 2 mm, 8 mm and 10 mm thickness parts. The U-shaped aluminum frames in the shoulder pitch-yaw and in the elbow pitch structures (see Section V) are built bending 90 deg the 2 mm thickness flat profile sections. The frame structure has been designed in such a way that the cost and complexity of the manufacturing processes is reduced as much as possible.

TABLE 3. Specifications of the compliant dual arm.

Total weight	1.3 *kg* (*with grippers*)
	Forearm length: 250 *mm*
Dimensions	*Upper arm length*: 250 *mm*
	Arms separation: 300 *mm*
Max. lift load	0.2 *kg per arm*
Rotation range	$\pm 90, [-30, 90], \pm 90, \pm 120$ *deg*
Joint deflection	± 30 *deg* (*approx.*)

TABLE 4. Specifications of the joints of the arms.

Joint	Servo model	Stall torque [N·m]	Joint stiffness [N·m/rad]	Rotation range [deg]
Shoulder pitch	DRS-0201	2.34	2.93	± 90
Shoulder roll	DRS-0201	2.34	2.1	[-30, 90]
Shoulder yaw	DRS-0101	1.17	0.8	± 90
Elbow pitch	DRS-0201	2.34	1.48	± 120

The main specifications of the dual arm manipulator are summarized in TABLE 3, providing additional information relative to each joint of the arms in TABLE 4. The maximum lift load was obtained placing a payload mass at the grippers with the arm fully stretched, rotating it from the vertical to the horizontal position so the torque due to gravity is maximum. The kinematic configuration, described in more detail in the following subsection, as well as the dimensions are similar to the human arm motivated by the convenience of having human-like manipulation capabilities in an aerial platform. The shoulder roll joints are used for lifting the arms above the landing gear before the landing maneuver. Finally, two Futaba S3003 servos have been employed for building a simple gripper, integrating a micro switch in the palm for detecting the contact with the object to grasp.

The developed manipulator satisfies the following design requirements imposed in the first stage of the design process:

1) Low weight and inertia.
2) Mechanical robustness, with high servo protection.
3) Intersection of the four joint axes in a common point, which simplifies the inverse kinematics.

4) Integration of compliant transmission mechanism.
5) Integration of deflection potentiometers in the joints.
6) Low clearance for increasing the accuracy in the positioning of the end effector.

All these features contribute to increase the probability of success in the application of an aerial manipulation robot to inspection and maintenance tasks in outdoor environments.
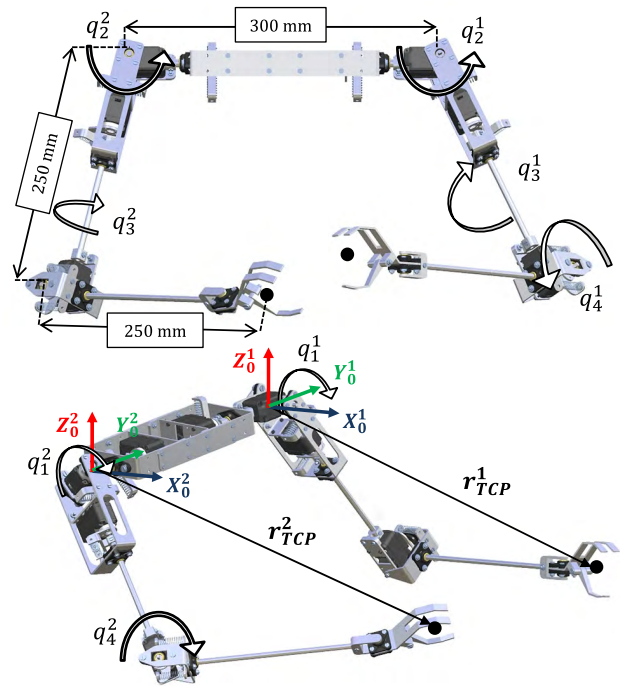
FIGURE 6. Kinematic configuration of the anthropomorphic dual arm and reference frames of both arms attached to the shoulder joint.

B. KINEMATICS

1) KINEMATIC CONFIGURATION

The anthropomorphic dual arm provides 4 DOF's for end effector positioning in a human-like kinematic configuration with the shoulder pitch joint at the base, followed by the shoulder roll, shoulder yaw and the elbow pitch joint. The corresponding joint variables of the output links are denoted by q_1^i, q_2^i, q_3^i, and q_4^i, respectively, with $i = 1, 2$ for the left and right arms. The wrist orientation joints have not been implemented in this version. A rendered view of the arms with the parameters of the kinematic model is represented in **Fig. 6**, including the forearm and upper arm lengths, the separation between the arms, and the joint angles with the positive direction of rotation given by the right-hand criteria. A reference frame $X_0^i Y_0^i Z_0^i$ attached to the intersection point of the joints of the shoulder of each arm is defined, so the tool center point (TCP) or any point in the workspace will be referenced to this frame. Each arm provides one redundant DOF that can be exploited for collision avoidance, null space control, or for orienting the end effector. In this work the shoulder roll angle is considered as a parameter, $q_2^i = \varphi_i$, which can

be tuned according to the task. For example, in the take-off or landing operations, the arms should be in a position such that the elbow and wrist points are above the landing gear, so $\varphi_i = \pm 90$ degrees, whereas in a visual servoing task, this angle will take values around $\varphi_i = \pm 10$ degrees.

2) FORWARD KINEMATICS
Let $FK_i : \Re^4 \rightarrow \Re^3$ represents the forward kinematics of the i-th arm. The position of the TCP of each arm is obtained multiplying the transformation matrices associated to each joint, defined as follows:

$$
{}^0_1T_i\left(q_1^i\right) = \begin{bmatrix} c_1^i & 0 & s_1^i & 0 \\ 0 & 1 & 0 & 0 \\ -s_1^i & 0 & c_1^i & 0 \\ 0 & 0 & 0 & 1 \end{bmatrix}
$$

$$
{}^1_2T_i\left(q_2^i\right) = \begin{bmatrix} 1 & 0 & 0 & 0 \\ 0 & c_2^i & -s_2^i & 0 \\ 0 & s_2^i & c_2^i & 0 \\ 0 & 0 & 0 & 1 \end{bmatrix}
$$

$$
{}^2_3T_i\left(q_3^i\right) = \begin{bmatrix} c_3^i & -s_3^i & 0 & 0 \\ s_3^i & c_3^i & 0 & 0 \\ 0 & s_2^i & 1 & 0 \\ 0 & 0 & 0 & 1 \end{bmatrix}
$$

$$
{}^3_4T_i\left(q_4^i\right) = \begin{bmatrix} c_4^i & 0 & s_4^i & 0 \\ 0 & 1 & -s_2^i & 0 \\ -s_4^i & 0 & c_4^i & -L_1 \\ 0 & 0 & 0 & 1 \end{bmatrix} \quad (2)
$$

Here $c_j^i = \cos(q_j^i)$ and $s_j^i = \sin(q_j^i)$. The upper arm link length (from shoulder to elbow) and the forearm length (from elbow to TCP) are denoted by L_1 and L_2, respectively. The last transformation matrix is referred to the elbow joint, so it is displaced the upper arm link length L_1. The position of the TCP referred to each frame is computed as follows:

$$
r_{TCP}^i\left(q^i\right) = \begin{bmatrix} x_i \\ y_i \\ z_i \end{bmatrix} = FK_i\left(q^i\right)
$$

$$
= \left(\prod_{j=1}^{4} {}^{j-1}_j T\left(q_j^i\right)\right) \cdot \begin{bmatrix} 0 \\ 0 \\ -L_2 \\ 1 \end{bmatrix} \quad (3)
$$

where $q^i = [q_1^i, q_2^i, q_3^i, q_4^i]^T$ is the angular position vector of the output link, denoting as $\theta^i = [\theta_1^i, \theta_2^i, \theta_3^i, \theta_4^i]^T$ the servo position vector.

3) INVERSE KINEMATICS
In order to provide an analytical solution to the inverse kinematics, it was imposed by design that the rotation axis of all the joints intersect in a common point. The joint angles of the output links can be determined from the desired Cartesian

position applying the inverse kinematics $IK_i : R^3 \rightarrow R^4$:

$$
IK_i\left(r_{TCP}^i\right) = FK_i^{-1}\left(r_{TCP}^i\right) = \begin{bmatrix} q_1^i \\ q_2^i \\ q_3^i \\ q_4^i \end{bmatrix} \quad (4)
$$

As mentioned before, it is imposed for simplicity that $q_2^i = \varphi_i$, considering the angle φ_i as a parameter. The elbow pitch angle only depends on the position of the TCP and on the forearm and upper arm links lengths:

$$
q_4^i = -cos^{-1}\left(\sqrt{\frac{x_i^2 + y_i^2 + z_i^2 - L_1^2 - L_2^2}{2 \cdot L_1 \cdot L_2}}\right) \quad (5)
$$

It can be demonstrated that the shoulder pitch joint satisfies the following trigonometric equation whose analytical solution is omitted for space reasons:

$$
x^i \cdot sin\left(q_1^i\right) + z^i \cdot \cos\left(q_1^i\right) w_i \quad (6)
$$

$$
w_i = \frac{L_2^2 - (L_1^2 + x_i^2 + z_i^2) + 2 \cdot L_1 \cdot y_i \cdot \sin\left(q_2^i\right)}{2 \cdot L_1 \cdot \cos\left(q_2^i\right)} \quad (7)
$$

Note however that the resulting quadratic equation may have two solutions, corresponding to the elbow-up/down poses. The shoulder yaw angle is finally obtained:

$$
q_3^i = atan2\left(a^i, b^i\right) \quad (8)
$$

$$
a^i = x_i \cdot s_1^i \cdot s_2^i + y_i \cdot c_2^i + z_i \cdot c_1^i \cdot s_2^i \quad (9)
$$

$$
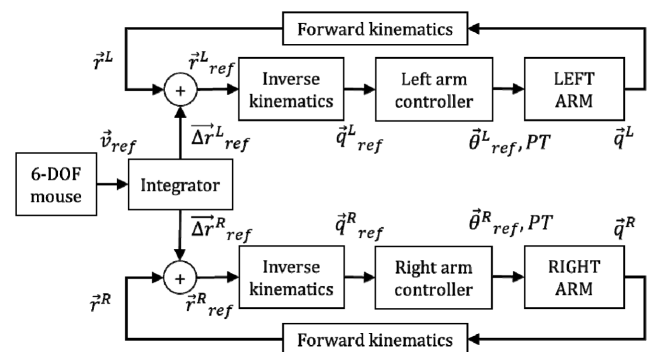b^i = x_i \cdot c_1^i - z_i \cdot s_1^i \quad (10)
$$

FIGURE 7. Cartesian position/velocity controller based on inverse kinematics.

C. ARMS CONTROL BASED IN INVERSE KINEMATICS
A position/velocity controller based on inverse kinematics has been implemented. The block diagram can be seen in **Fig. 7**. In this example, the arms are operated using a 6-DOF mouse that generates the velocity references, although this scheme has been also applied to visual servoing. The inverse kinematics module generates then the joint references taken as input by the low level arms controller, giving as output the reference position and play time (PT) sent to the servos.

The proposed scheme exploits the controller embedded in all the Herkulex smart servos, which generates a trapezoidal velocity profile for reaching the goal position in the desired play time. Smooth trajectories can be achieved imposing that the position references are sent at the midpoint of the velocity profile.
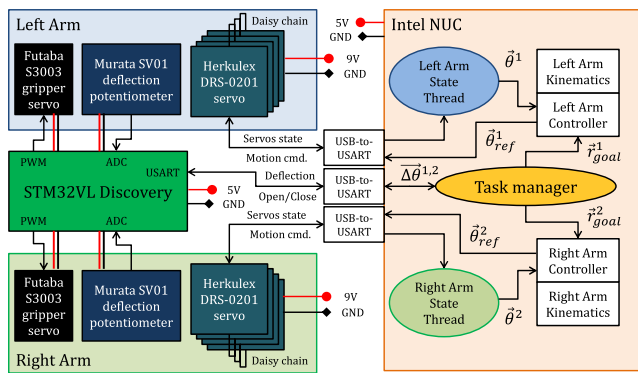

FIGURE 8. Components and architecture of the compliant dual arm.

D. HARDWARE/SOFTWARE ARCHITECTURE

The architecture of the compliant dual arm manipulator is depicted in **Fig. 8**. The components of each arm are the four Herkulex servos indicated in TABLE 4, the Murata SV 01A deflection potentiometers attached to the joints, and a Futaba S3003 servo used in the gripper. The servos on each arm are connected in daisy chain to the Intel NUC board through an USB-to-USART device. As all the servos share the same TTL bus, the command/read rate is set to 50 Hz in order to prevent high packet loss. The analog signals provided by the deflection potentiometers are converted by the Analog to Digital Converter (ADC) in the STM32VL Discovery microcontroller board, which also generates the PWM signals that control the servos of the grippers. The microcontroller board, programmed in C using the Atollic True Studio IDE, is also connected to the Intel NUC computer through the USART interface. The control program executed in this board over Ubuntu 14.04 was developed in C/C++, making use of the cmake tool in order to facilitate the portability of the software project between different computer boards. The higher level class of the program is the Task Manager, which implements several tasks or routines that can be selected by the operator from the Ground Control Station (GCS). The task manager gathers information from the state of the arms from the corresponding threads, providing the reference trajectories to the left/right arm controllers. These modules make use of the inverse kinematic model described previously for obtaining the joint references sent to the embedded servo controller through the USART interface.

IV. COMPLIANT JOINT WITH DEFLECTION FEEDBACK
A. BENEFITS OF MECHANICAL JOINT COMPLIANCE
In most industrial manipulators, the torque is estimated from the current injected to the motor, or measuring the micro

deflections of an aluminum structure attached between the motor shaft and the output link employing strain gauges. However, current-based torque estimation and control lacks of accuracy due to the friction of the gearbox, and torque sensors based on strain gauges require special electronics and a calibration process which increases the cost of the devices. What is more, although joint compliance and even variable stiffness/impedance can be achieved at software level controlling the torque at high rate ($\sim$1 KHz), the joint is intrinsically stiff and therefore less safe than a mechanically compliant joint in an environment shared with humans.
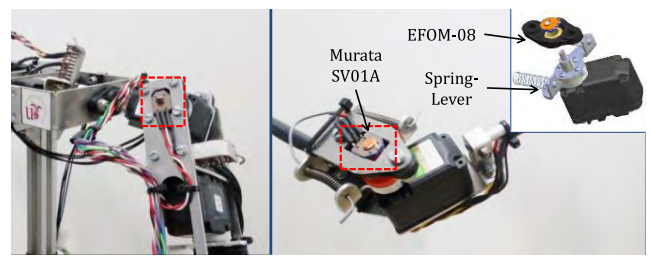

FIGURE 9. Deflection potentiometer integrated in the shoulder roll (left) and in the elbow pitch joints (right).

Introducing flexible elements like springs or elastomers for transmitting the motion of the motor to the output link is a simple and low cost method for providing compliance at hardware level. These components act as low pass filters, absorbing the energy of impacts and overloads in a passive way thanks to their natural dampening. This feature results of special interest for protecting the servo actuators against peak torques in those situations in which the manipulator enters in contact with the environment. A potentiometer or encoder can be introduced in the compliant joint for building a simple torque sensor based on the deflection of the springs. This idea was previously introduced in the 3-DOF compliant arm prototype, demonstrating experimentally its application to force control in [26]. **Fig. 9** shows two compact Murata SV01A potentiometers integrated in the frame structure of two joints of the developed dual arm system. A D-shaped shaft attached to the servo horn is inserted in the hollow shaft of the potentiometer for measuring the relative rotation of the output link with respect to the servo shaft.

B. SPRING-LEVER TRANSMISSION MECHANISM
1) MECHANICS
Two of the main requirement imposed in the arms design, mechanical joint compliance and servo protection, have been implemented employing the igubal EFOM-08 and EFSM-06 flange bearings manufactured by igus. These components provide excellent features that can be exploited in the design of low weight robotic arms: low mass density w.r.t. steel bearings (1.4 g/cm^3 *vs* 8.5 g/cm^3), low friction, maintenance free, high axial and radial load support, and high impact and thermal resistance. Also the pivot angle of the ball is useful for compensating the misalignment errors associated
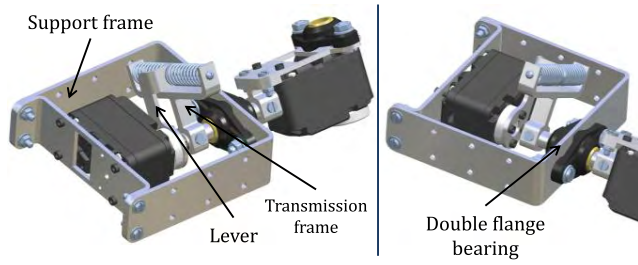
FIGURE 10. Shoulder pitch spring-lever mechanism. Full servo protection.

to the bending of the aluminum frames. **Fig. 10** shows the EFOM-08 flange bearings installed in the shoulder pitch and elbow pitch structures. The double flange bearing in side-by-side configuration provides full isolation of the servo against axial/radial loads introduced by the crossing shaft. The low friction and damping of the iglidur W300 plastic allows the smooth rotation of the shaft.

The spring-lever transmission mechanism consists of a pair of compression springs that transmit the motion of the servo shaft to the output link. The L-shaped lever frame is screwed to the servo horn, pushing the springs that push the T-shaped transmission frame of the output link. The design parameters of this mechanism are the lever length and the stiffness of the springs. The torque-deflection characteristic is described in more detail in [26]. The torsional stiffness of the compliant joint is obtained in the following way:

$$\tau_j^i \cong K_j^i \cdot \left(l_j^i\right)^2 \cdot \Delta\theta_j^i = k_j^i \cdot \Delta\theta_j^i \quad (11)$$

where K_j^i is the stiffness of the compression spring, l_j^i is the lever length, k_j^i is the equivalent torsional stiffness, and $\Delta\theta_j^i$ is the deflection of the j-th joint of the i-th arm, defined as:

$$\Delta\theta_j^i = \theta_j^i - q_j^i \quad (12)$$

This angle is measured by the potentiometer attached at the frame structure, as depicted in **Fig. 9**, allowing the estimation and control of the torque.

2) COMPLIANT JOINT DYNAMICS

The dynamic model of a compliant joint actuator consists of two parts, the servo-side and the output link-side dynamics, related through the torque transmitted by the spring-lever transmission mechanism. Let us consider an arbitrary joint, omitting the indices for clarity in the notation. If τ_m, τ_f, and τ represent the torque generated by the motor, the friction of the gearbox, and the torque transmitted to the output link, then the following balance equation can be stablished:

$$\tau_m = b\ddot{\theta} + \tau_f + \tau \quad (13)$$

where b is the inertia of the rotor. That is, the torque of the servo motor is spent in accelerating the rotor, compensating the friction, and pushing the output link. On the other hand, the output link will be affected by external forces/torques due to contacts, impacts or motion constraints, the gravity,

and by the torque introduced from the compliant transmission mechanism:

$$J\ddot{q} + mgLsin\left(q\right) = \tau + \tau_{ext} \quad (14)$$

Here m, J, and L are the mass, inertia, and length of the link respectively, whereas g is the gravity constant. Note that the common term in equations (14) – (15) is the transmitted torque τ. Taking into account equations (12) – (13), and the damping due to the friction of the output link shaft with the flange bearing, the joint torque can be computed as follows:

$$\tau = k\left(\theta - q\right) + d\left(\dot{\theta} - \dot{q}\right) = k \cdot \Delta\theta + d \cdot \Delta\dot{\theta} \quad (15)$$

where d is the joint damping. This equation shows that the torque can be estimated from the joint position and velocity signals provided by the servo and the deflection sensor. It is necessary to remark that most low cost servos only accept as input position references, but torque estimation and control can be achieved thanks to the deflection of the springs.

The Herkulex servos were experimentally characterized in the time and frequency domains, concluding that a first-order dynamics with delay models properly the actuator:

$$G\left(s\right) = \frac{\theta}{\theta_{ref}} = \frac{e^{T_{delay}\cdot s}}{1 + T_{servo} \cdot s} \quad (16)$$

where $T_{delay} = 0.02[s]$ is the time delay associated to the serial interface, and $T_{servo} = 0.035[s]$ is the time constant.

3) DUAL ARM MANIPULATOR DYNAMICS

The dynamic model of a compliant joint manipulator can be expressed in the usual matrix form, obtaining the equations of motion from the Euler-Lagrange method based on the Lagrangian and the generalized equation of the forces and torques. References [30] and [31] can be followed for a more in detail description of the modeling and control of compliant joint manipulators.

As in the single joint case, the equations of the dynamic model of a compliant joint arm can be divided into two parts. Firstly, the servo-side dynamics includes the torque of the motor, the friction of the gearbox, the torque transmitted by the spring-lever mechanism, and the inertia of the rotor:

$$\tau_m^i = B_i\left(\theta^i\right)\ddot{\theta}^i + \tau_f^i + \tau^i \quad (17)$$

Here $B_i \in \mathbb{R}^{4\times4}$ is the servo inertia matrix, and τ_m^i, τ_f^i, and $\tau^i \in \mathbb{R}^4$ are the motor, friction and transmitted torques of the i-th arm. Now, the output link dynamics includes the inertia, Coriolis and centrifugal terms, and the gravity component:

$$M_i\left(q^i\right)\ddot{q}^i + C_i\left(q^i,\dot{q}^i\right) + G_i\left(q^i\right) = \tau^i + \tau_{ext}^i \quad (18)$$

where $M_i \in \mathbb{R}^{4\times4}$ is the output link inertia matrix, C_i and $G_i \in \mathbb{R}^4$ are the Coriolis and gravity terms, respectively, and $\tau_{ext}^i \in \mathbb{R}^4$ is the torque due to external forces exerted over the

i-th arm. The common term in (17) and (18) is the torque $\boldsymbol{\tau}^i$ which can be estimated from the joint deflection:

$$\boldsymbol{\tau}^i = \boldsymbol{K}^i\left(\boldsymbol{\theta}^i - \boldsymbol{q}^i\right) + \boldsymbol{D}^i\left(\dot{\boldsymbol{\theta}}^i - \dot{\boldsymbol{q}}^i\right) = \boldsymbol{K}^i \Delta \boldsymbol{\theta}^i + \boldsymbol{D}^i \Delta \dot{\boldsymbol{\theta}}^i$$

(19)

where $\boldsymbol{K}^i = diag(k_j^i)$ and $\boldsymbol{D}^i = diag(d_j^i) \in \mathbb{R}^{4 \times 4}$ are the joint stiffness and damping matrices, respectively.

C. AERIAL MANIPULATOR DYNAMICS

The derivation of the complete dynamic model of a dual arm aerial manipulator is out of the scope of this work, although previous research in dual arm space manipulators [32] and underwater manipulators [33] are suggested. In our previous work [28] we developed the equations of the Euler-Lagrange formulation for a stiff-joint dual arm aerial robot, expressed in the usual matrix form with the inertia, Coriolis and gravity terms. In the case of the compliant manipulator described in this paper, the vector of generalized coordinates $\boldsymbol{\xi} \in \mathbb{R}^{22}$ includes both the servo and the output link angular position vectors, as well as the UAV position and attitude vectors, $\boldsymbol{r}$ and $\boldsymbol{\eta} \in \mathbb{R}^3$, respectively:

$$\boldsymbol{\xi} = \left[\boldsymbol{r}^T \; \boldsymbol{\eta}^T \; \boldsymbol{\theta}^{1,T} \; \boldsymbol{q}^{1,T} \; \boldsymbol{\theta}^{2,T} \; \boldsymbol{q}^{2,T} \right]^T$$

(20)

The vector of generalized forces $\boldsymbol{\Gamma} \in \mathbb{R}^{22}$ includes the forces and torques acting over the aerial platform, $\boldsymbol{F}_{UAV}$ and $\boldsymbol{\tau}_{UAV} \in \mathbb{R}^3$, the torque $\boldsymbol{\tau}^i$ transmitted by the motors, and the external torque $\boldsymbol{\tau}_{ext}^i$ acting over the output links:

$$\boldsymbol{\Gamma} = \left[\boldsymbol{F}_{UAV}^T \; \boldsymbol{\tau}_{UAV}^T \; \boldsymbol{\tau}^{1,T} \; \boldsymbol{\tau}_{ext}^{1,T} \; \boldsymbol{\tau}^{2,T} \; \boldsymbol{\tau}_{ext}^{2,T} \right]^T$$

(21)

The equations of the dynamic model are obtained from the Lagrangian L and the generalized equation of the forces and torques.

$$\frac{d}{dt}\left\{\frac{\partial L}{\partial \dot{\boldsymbol{\xi}}}\right\} - \frac{\partial L}{\partial \boldsymbol{\xi}} = \boldsymbol{\Gamma}; \; L = K - V$$

(22)

where K and V are the kinetic and potential energy of the system, respectively. Note that the potential energy includes two terms, the gravitational potential and the elastic potential energy associated to the flexible joints, which depends on the joint stiffness and the deflection angle. After some work, it is possible to express the model in the following matrix form:

$$\boldsymbol{M}\left(\boldsymbol{\xi}\right)\ddot{\boldsymbol{\xi}} + \boldsymbol{C}\left(\boldsymbol{\xi},\dot{\boldsymbol{\xi}}\right) + \boldsymbol{G}\left(\boldsymbol{\xi}\right) + \boldsymbol{K}\left(\boldsymbol{\xi}\right) + \boldsymbol{D}\left(\boldsymbol{\xi},\dot{\boldsymbol{\xi}}\right) = \boldsymbol{\Gamma}$$

(23)

where $\boldsymbol{M} \in \mathbb{R}^{22 \times 22}$ is the generalized inertia matrix, $\boldsymbol{C} \in \mathbb{R}^{22}$ represents the centrifugal and Coriolis terms, $\boldsymbol{G} \in \mathbb{R}^{22}$ is the gravity component of the wrenches, whereas $\boldsymbol{K}$ and $\boldsymbol{D} \in \mathbb{R}^{22}$ are the components associated to the deflection and the friction of the compliant joints. According to the notation, all these terms depend on the generalized coordinate vector, or well on a specific group of coordinates. The position of the manipulator relative to the base of the aerial platform and the angular position of the links modifies the value of the inertia matrix and the thrust that the propellers should deliver to compensate the torque due to gravity when the

center of mass is displaced. In general, it is convenient that the manipulator is as close as possible to the geometric center of the UAV, maintaining the symmetry in the mass distribution, although from the theoretical point of view, the particular location of the arms does not affect the model.
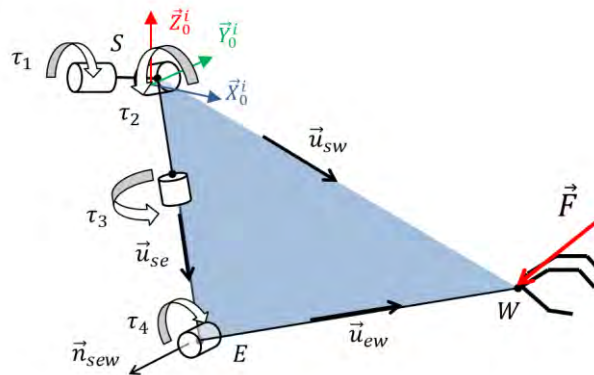

FIGURE 11. Geometric model considered for deriving the force-torque relationships.

D. FORCE-TORQUE RELATIONS

1) GEOMETRIC INTERPRETATION

In many manipulation operations it is necessary to estimate and control the contact forces at the end effector. This can be done measuring the deflection of the joints and applying the force-torque relations. These can be obtained in two steps: 1) compute the torque vector $\boldsymbol{\tau}_j^i = \boldsymbol{F}_j^i \times \boldsymbol{r}_j^i$ for all the joints, that is, the cross product between the force acting over the link of the joint and its position, and 2) project the torque on the corresponding joint axis. The matrix representation is then obtained. Let consider the diagram shown in **Fig. 11**, where S, E and W are the shoulder, elbow and wrist points referred to frame $\boldsymbol{0}^i$ attached to the shoulder joint. These points, whose position vectors are $\boldsymbol{r}_s = \boldsymbol{0}$, $\boldsymbol{r}_e$ and $\boldsymbol{r}_w$, define the *SEW* plane and the normal vector $\boldsymbol{n}_{sew}$. The elbow and wrist points are obtained from the forward kinematic model. From now on, superscript i is omitted for clarity in the notation. The normalized position vectors shoulder-elbow and elbow-wrist are denoted by $\boldsymbol{u}_{se}$ and $\boldsymbol{u}_{ew}$, and are defined as follows:

$$\boldsymbol{u}_{se} = \frac{\boldsymbol{r}_e}{\|\boldsymbol{r}_e\|}$$

(24)

$$\boldsymbol{u}_{ew} = \frac{\boldsymbol{r}_w - \boldsymbol{r}_e}{\|\boldsymbol{r}_w - \boldsymbol{r}_e\|}$$

(25)

The normal vector to the *SEW* plane can be computed as:

$$\boldsymbol{n}_{sew} = \frac{\boldsymbol{u}_{se} \times \boldsymbol{u}_{ew}}{\|\boldsymbol{u}_{se} \times \boldsymbol{u}_{ew}\|}$$

(26)

It will be assumed that the contact force $\boldsymbol{F}$ is applied at the wrist point. The torque supported by the elbow pitch and the shoulder yaw joints is firstly obtained from the vector:

$$\boldsymbol{\tau}_{ew} = \boldsymbol{F} \times (\boldsymbol{r}_w - \boldsymbol{r}_e)$$

(27)

Now, the projection of this torque vector in the direction of the rotation axis of each joint provides the corresponding joint torque. In the case of the elbow joint, the direction of rotation is parallel to $\boldsymbol{n}_{sew}$ and thus:

$$\tau_4 = \boldsymbol{n}_{sew}^T \cdot \boldsymbol{\tau}_{ew} \qquad (28)$$

The axis of rotation of the shoulder yaw joint is $\boldsymbol{u}_{se}$, so:

$$\tau_3 = \boldsymbol{u}_{se}^T \cdot \boldsymbol{\tau}_{ew} \qquad (29)$$

The torque in the shoulder roll and pitch joints is obtained in a similar way, considering the shoulder-to-wrist vector and the direction of rotation of these joints:

$$\boldsymbol{\tau}_{sw} = \boldsymbol{F} \times \boldsymbol{r}_w \qquad (30)$$
$$\tau_2 = [\cos q_1, 0, \sin q_1] \cdot \boldsymbol{\tau}_{sw} \qquad (31)$$
$$\tau_1 = [0, 1, s0] \cdot \boldsymbol{\tau}_{sw} \qquad (32)$$

Equations (28) – (32) can be rewritten in matrix form, in such a way that torque-force relation is linear. This is done expressing the cross product as matrix multiplication using a skew-symmetric matrix defined as follows:

$$\boldsymbol{F} \times \boldsymbol{r} = \boldsymbol{F} \times \begin{bmatrix} r_x \\ r_y \\ r_z \end{bmatrix} = \begin{bmatrix} 0 & -r_z & r_y \\ r_z & 0 & -r_x \\ -r_y & r_x & 0 \end{bmatrix} \cdot \boldsymbol{F} = \boldsymbol{A} \cdot \boldsymbol{F} \qquad (33)$$

2) JACOBIAN-BASED INTERPRETATION

The force at the end effector can be computed from the joint torque and the Jacobian of the manipulator. Assuming that the contact force control task is executed in static or close to static conditions, the torque can be computed easily from the joint deflection and the joint stiffness matrix (neglecting the damping), so the force vector in task space will be given by:

$$\boldsymbol{F}^i = \left(\boldsymbol{J}^{i,T}\right)^{-1} \boldsymbol{\tau}^i = \left(\boldsymbol{J}^{i,T}\right)^{-1} \boldsymbol{K}^i \Delta\boldsymbol{\theta}^i \qquad (34)$$

Here $\boldsymbol{J}^i \in \mathbb{R}^{3\times4}$ is the Jacobian of the i-th manipulator, and $\boldsymbol{K}^i = diag(k_j^i) \in \mathbb{R}^{4\times4}$ is the corresponding joint stiffness matrix.

3) CARTESIAN DEFLECTION

It is interesting to note that, if $\boldsymbol{q}^i$ is replaced by $\boldsymbol{\theta}^i$ in Equation (3), then $\boldsymbol{FK}_i(\boldsymbol{\theta}^i)$ would represent the forward kinematics of an equivalent stiff joint manipulator. The difference between the position of the TCP in this virtual manipulator and in the compliant arm is defined as the Cartesian deflection, $\Delta\boldsymbol{l}^i$:

$$\Delta\boldsymbol{l}^i = \boldsymbol{FK}_i(\boldsymbol{\theta}^i) - \boldsymbol{FK}_i\left(\boldsymbol{q}^i\right) \qquad (35)$$

The Cartesian deflection represents the deviation in the position of the TCP due to the deflection of the compliant joints. This concept is useful if, for example, a camera head gives the 3D position of a marker attached at the end effector, as it would allow the estimation and control of contact forces directly in the task space, increasing at the same time the
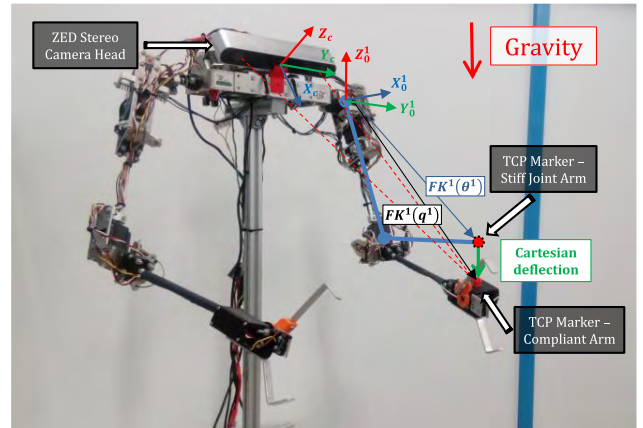
FIGURE 12. Cartesian deflection measured on the left arm by means of a red color marker attached at the TCP and a stereo camera head.

positioning accuracy. This has been represented in **Fig. 12**. In static conditions, the contact force will be proportional to the Cartesian deflection:

$$\boldsymbol{F}^i = \boldsymbol{K}_C^i \cdot \Delta \boldsymbol{l}^i \qquad (36)$$

where the Cartesian stiffness matrix $\boldsymbol{K}_C^i \in \mathbb{R}^{3\times3}$ is obtained from the joint stiffness matrix and the Jacobian:

$$\boldsymbol{K}_C^i = \left(\boldsymbol{J}^{i,T}\right)^{-1} \boldsymbol{K}_s^i \left(\boldsymbol{J}^i\right)^{-1} \qquad (37)$$

According to this equation, the Cartesian stiffness will vary with the position of the joints. In particular, infinite stiffness is associated to the kinematic singularities of the arms.
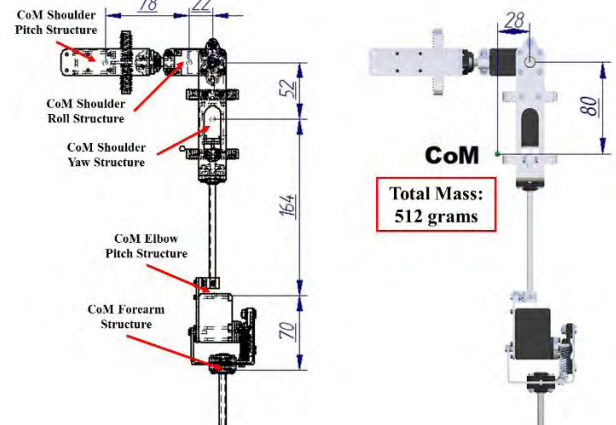
FIGURE 13. Relative distances between the center of mass of the links (left) and global center of mass of the left arm (right). Lenghts in mm.

V. ARMS FRAME STRUCTURE

This section details the construction of the different links of the arms, providing the mass and inertia parameters obtained from the CAD model, which are summarized in **Fig. 13** and TABLE 5. The definition of the XYZ axes associated to the CoM of each structure is shown in the figures below. This

Structure	Mass	I_{xx}	I_{yy}	I_{zz}	I_{xy}	I_{xz}	I_{yz}
	g	g·cm²	g·cm²	g·cm²	g·cm²	g·cm²	g·cm²
Sh. Pitch	127	853	750	1491	84	0	0
Sh. Roll	101	714	216	772	58	0	0
Sh. Yaw	121	1354	1813	611	0	38	0
E. Pitch	87	2055	2017	117	0	-79	-10
Forearm	53	1318	1187	177	0	0	-95

section does not consider the mass and inertia of the spring-lever transmission frames as these parameters are negligible w.r.t. the corresponding output links.
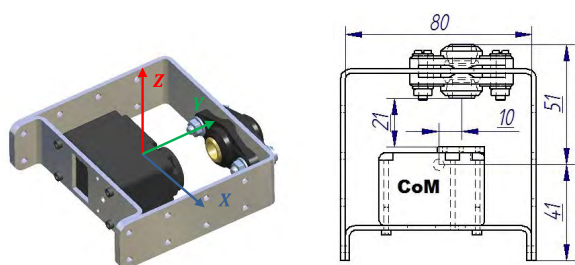
FIGURE 14. CoM and dimensions (in mm) of the shoulder pitch structure.

A. SHOULDER PITCH STRUCTURE

This structure provides full protection to the Herkulex DRS-0201 servo. The radial and axial loads are supported by the igubal EFOM-08 flange bearings installed in side-by-side configuration, allowing the rotation of the shaft that connects the shoulder roll structure with the compliant transmission mechanism of the shoulder pitch joint. These components also provide vibration dampening and smooth rotation of the shaft. **Fig. 14** shows a rendered view of this structure along with the XYZ axes to which the inertia moments are referred, as well as the dimensions in mm. The structure is built from two U-shaped aluminum parts manufactured by laser cut, 2 mm thickness and 25 mm width. The space left between the servo horn and the inner flange bearing (21 mm) is allocated for installing the spring lever mechanism and the deflection potentiometer. The assembly of the spring lever mechanism and the shoulder roll structure can be seen in **Fig. 10**.

B. SHOULDER ROLL STRUCTURE

This structure, whose rendered view is depicted in **Fig. 15**, provides partial protection to the Herkulex DRS-0201 servo through an igubal EFOM-08 flange bearing installed over the aluminum support frame on the back of the actuator. The shoulder yaw structure, described in next sub-section, is supported by this flange bearing and by the servo horn. The 8 mm Ø shaft crosses the EFOM-08 pair at the shoulder pitch structure, connecting the shoulder pitch transmission with the
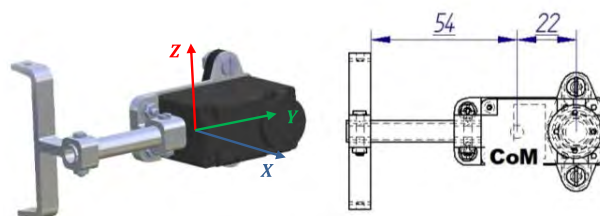
FIGURE 15. CoM and dimensions (in mm) of the shoulder roll structure.

shoulder roll support frame. The shaft fits in a T-shaped frame in such a way that there is no clearance causing a dead-zone at the end effector.
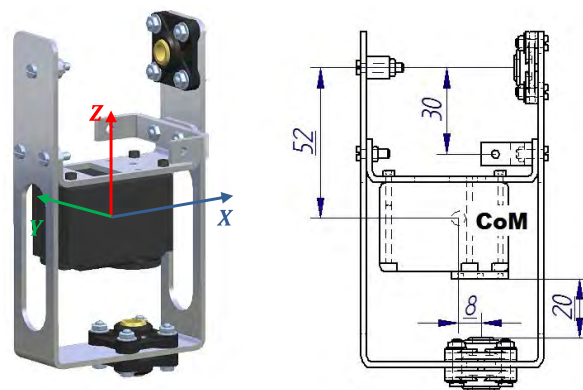
FIGURE 16. CoM and dimensions (in mm) of the shoulder roll structure.

C. SHOULDER YAW STRUCTURE

A pair of igubal EFSM-06 flange bearings screwed into the base of a U-shaped frame support the rotation of the upper arm link and the compliant transmission. A third component attached to the inner side of the frame allows the rotation of this structure around the shoulder roll shaft, whereas the 8 mm Ø shaft in the opposite side is inserted in the EFOM-08 flange bearing of the shoulder roll structure. A rendered view of the assembly and the dimensions can be seen in **Fig. 16**.
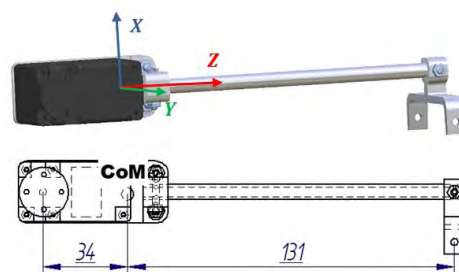
FIGURE 17. CoM and dimensions (in mm) of the shoulder roll structure.

D. UPPER ARM LINK

This assembly, shown in **Fig. 17**, is similar to the shoulder roll structure, although in this case the transmission frame on

the right of the 6 mm Ø profile is rotated 90 deg with respect to the servo support frame. This shaft passes through the pair of EFSM-06 flange bearings of the shoulder yaw structure. This solution, in which the elbow pitch servo is placed at the elbow joint, is not convenient in terms of inertia, but it avoids introducing a transmission mechanism, reducing the weight and complexity in the design and the assembly.
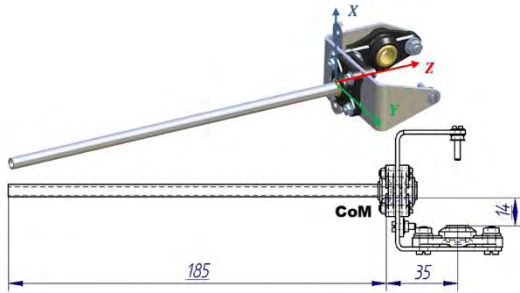

FIGURE 18. CoM and dimensions (in mm) of the forearm structure.

E. FOREARM LINK

The forearm link consists of a 6 mm Ø link connected to the elbow joint through a U-shaped frame and a pair of EFSM-06 flange bearings in side-by-side configuration. A rendered view of the assembly is represented in **Fig. 18**. The EFOM-08 flange bearing is inserted into the servo shaft, as **Fig. 9** shows, using a M3 screw on the opposite side as second support point in the elbow pitch base frame. Although the current version does not implement the wrist orientation mechanism, the EFSM-06 pair allows the rotation of the end effector around the axis defined by the forearm link (wrist roll angle).

VI. EXPERIMENTAL RESULTS

This section presents experimental results for characterizing and validating the developed anthropomorphic, compliant and lightweight dual arm manipulator. The resonance frequencies of the compliant joints are identified, showing the response to impacts against the end effector. Zero deflection control in grabbing situations and bimanual object grasping experiments have been also conducted. For clarity in the evaluation of the concepts of interest, the graphical results correspond to fixed base experiments, as the conditions for the outdoor flight tests are less controllable. Finally, bimanual grasping on flight has been demonstrated in outdoors.

A. FREQUENCY ANALYSIS

Each individual compliant joint can be assimilated to a mass-spring-damper system characterized by its natural frequency. In a compliant joint manipulator, the distribution of the mass will vary with the position of the joints, and so the resonance frequencies. Furthermore, the deflection of one joint may excite another joints due to dynamic coupling. The goal of this experiment is identifying these behaviors in the dual arm manipulator, introducing a chirp (or sweep) signal in the
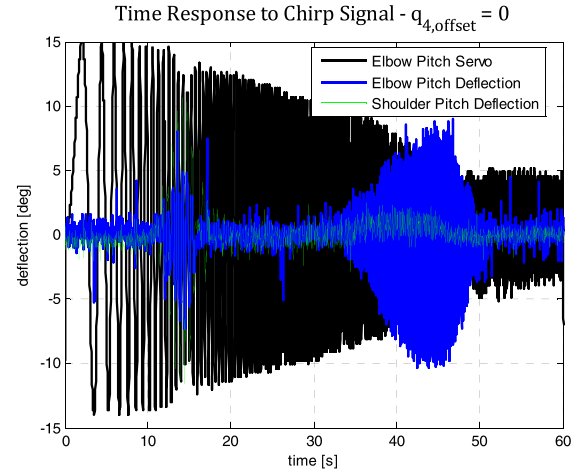
FIGURE 19. Elbow pitch (blue) and shoulder pitch (green) joint deflection for a 15 deg chirp signal generated by the elbow pitch servo (black).

elbow joint for this purpose. The elbow servo will generate a 15 deg amplitude oscillation, increasing the frequency linearly with the time from 0 up to 8 Hz in 60 seconds:

$$\theta_{4,ref}^{1,2}(t) = \theta_{4,offset}^{1,2} + 15 \cdot sin\left(\frac{8 \cdot \pi \cdot t^2}{60}\right) \tag{38}$$

Two representative configurations for the dual arm are considered depending on the offset angle of the elbow: arms fully stretched ($\theta_{4,offset}^{1,2} = 0\ deg$), and L-shaped flexion of the elbow ($\theta_{4,offset}^{1,2} = 90\ deg$.) **Fig. 19** shows the evolution of the elbow pitch servo position along with the elbow pitch and the shoulder pitch deflection signals. No filtering was applied to these signals. As it can be seen, two resonance modes are identified in $t = 12\ s$ and in $t = 45\ s$. The first one is coupled to the shoulder pitch joint, whereas the second one mainly affects to the elbow joint. It is interesting to note that, at the resonance frequency of the first mode, the relative phase of the elbow pitch deflection signal drops 180 deg with respect to the servo position. This can be appreciated more clearly in **Fig. 20**. As the amplitude of the servo rotation is similar to the joint deflection but with different sign, the apparent effect is that the forearm link is not oscillating, which is confirmed by visual inspection of the experiment.

The Fast Fourier Transform (FFT) algorithm was applied to the signals depicted in **Fig. 19** for obtaining a frequency representation of the servo bandwidth and the resonance peaks of the compliant joints. These can be identified clearly in **Fig. 21**. The first resonance mode ($f_1 = 1.624\ Hz$) affects to the elbow pitch and shoulder pitch joints, whereas the second mode ($f_2 = 5.92\ Hz$) only affects to the elbow joint and it has a wider bandwidth than the first one. The servo actuator is not able to follow the chirp reference from $f = 1.5 Hz$ due to its limitations in speed and torque.

The variation in the frequency response of the compliant arm due to the rotation of the elbow joint is evidenced in **Fig. 22**. In this case, as the distance from the center of mass of the arm to the shoulder joint is lower, the resonance frequency

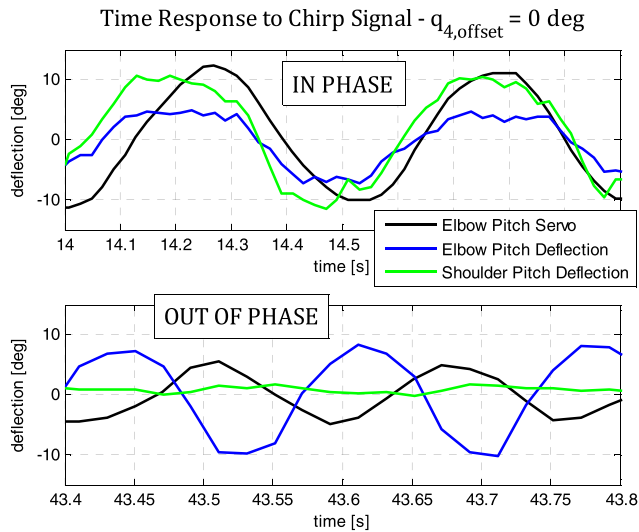## Time Response to Chirp Signal - $q_{4,offset}$ = 0 deg

FIGURE 20. Detailed view of the servo position and the joints deflection. Before the first resonance peak the deflection is in phase with the servo (up), dropping 180 deg in the second resonance peak (down).
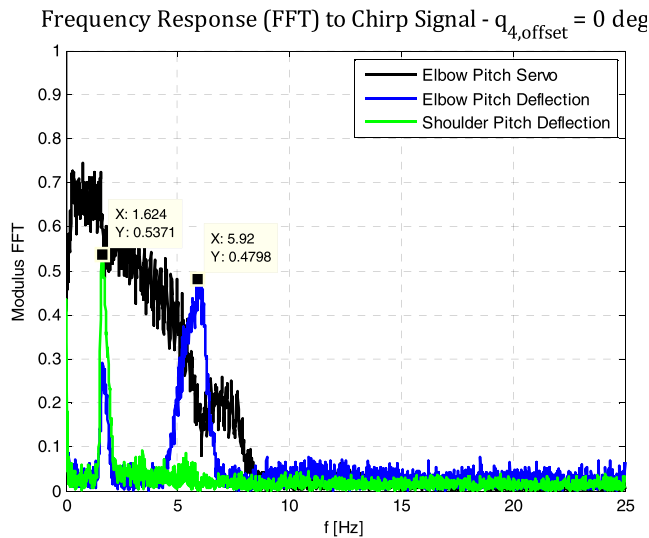
Frequency Response (FFT) to Chirp Signal - $q_{4,offset}$ = 0 deg

FIGURE 21. FFT applied to the elbow pitch servo (black) and to the elbow pitch (blue) and shoulder pitch (green) joint deflection. The resonance frequencies are identified at $f_1 = 1.6\ Hz$ and $f_2 = 5.9\ Hz$.

Frequency Response (FFT) to Chirp Signal - $q_{4,offset}$ = -90 de

FIGURE 22. FFT applied to the elbow pitch servo (black), the elbow pitch (blue) and shoulder pitch (green) joint deflection. The spectrum and resonance frequencies have changed along with the mass of the arm.
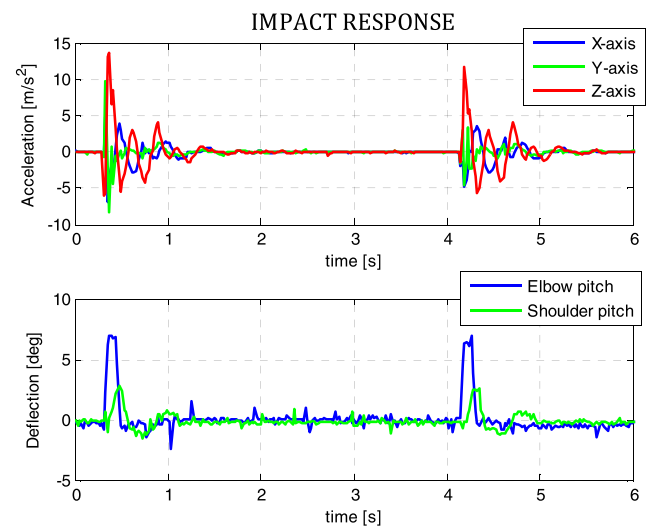
IMPACT RESPONSE

FIGURE 23. Impact response: acceleration at the TCP (up) and joints deflection (down).

increases, varying from $f_1 = 1.624\ Hz$ to $f_1 = 2.075\ Hz$. The amplitude of the second resonance mode is also higher due to the effect of gravity over the forearm link mass.

The identification of the resonance frequencies is useful for anticipating and preventing undesired behaviors of the aerial manipulator on flight, as these modes may be excited due to the dynamic coupling with the aerial platform or the control loop. Also the value of the joint damping can be determined experimentally from these figures, known the joint stiffness (TABLE 4) and link inertia (CAD model) parameters.

B. IMPACT RESPONSE

This experiment shows the response of the compliant joints when the end effector suffers the impact of a 62 g weight object thrown from a height of 57 cm, which corresponds to

a potential energy of 0.35 J. The setup consisted of a drylin T rail guide system TS-04-15 installed in vertical position, and a TW-04-15 carriage manufactured by igus® that slides along the rail. An accelerometer was attached under the end effector of the left arm (see **Fig. 4**), where the carriage will impact. **Fig. 23** represents the acceleration at this point and the deflection of the elbow pitch and shoulder pitch joints in two consecutive impacts. The reference position for these joints were $\theta_1^1 = 0$ and $\theta_4^1 = -90\ deg$. Note that the springs in the compliant joints act as low-pass filters, so the high frequency component of the energy generated by the impact is attenuated thanks to the natural damping of the springs and the bearing. This prevents that the shaft of the servos are damaged due to peak forces associated to the transition

from contactless to contact situations, improving the safety and robustness of the manipulator during the realization of tasks involving physical interaction with the environment.

C. ZERO DEFLECTION CONTROL IN CLOSED KINEMATIC CHAIN

Let us consider an operation in which the aerial manipulator has to grab a long bar using both arms. The bar is left on a bench in such a way that it is necessary to pull it upwards for retrieving it while the aerial platform is hovering in a fixed position above the bench. The motion constraints associated to grabbing situations may generate undesired forces that, when exerted over the aerial platform, will cause positioning drifts or even crashes if the UAV controller is not able to deal with them. What is more, the actuators in a stiff joint manipulator might be damaged if there is no torque feedback available to detect and compensate joint overloads. In order to reduce the influence of contact forces during grabbing phases, this work proposes a simple method that exploits the joint deflection in the developed manipulator. The idea is to implement a joint deflection controller that tries to maintain a zero deflection reference, or what is the same, a zero joint torque. With that, the manipulator will be able to compensate position deviations without disturbing the platform.

In this experiment, a low weight plastic box representing an inspection tool is grasped from a 35 cm length horizontal handle using both arms, forming a closed kinematic chain. A calibration process is previously executed for obtaining the voltage offset of the deflection potentiometers. After that, the zero deflection controller is enabled. A simple proportional controller provides the incremental joint position of the servos using the deflection feedback:

$$\theta_{j,ref}^i = \theta_j^i + K_p \cdot \Delta\theta_j^i \tag{39}$$

Here K_p is the proportional gain. When the grasped object is pulled or pushed by hand, the external force will cause the deflection of the joints. However, the elastic potential energy stored in the springs will be actively released by the servos, in such a way that the deflection will tend to zero. **Fig. 24** and **Fig. 25** represent the Cartesian position and the joint deflection of both arms when the object is guided following an elliptical trajectory over the XZ plane. **Fig. 26** shows the same signals when the object is guided in the X, Y and Z axes separately, which allows to identify the involved joints on each axis more clearly.

D. BIMANUAL GRASPING: OUTDOOR FLIGHTS

Outdoor flight tests were conducted for validating the dual arm design, demonstrating the bimanual grasping capability. The arms were integrated in a DJI Matrice 600 hexarotor for this purpose along with an Intel NUC computer board, a ZED stereo camera for visual servoing, a 5.8 GHz wireless link, and the batteries. The experiment consisted of six phases: 1) take off, 2) approach to the inspection tool installed on a PVC pipe, 3) move the arms to the operation position, 4) activate visual servoing, 5) retrieve the inspection tool, and 6) release
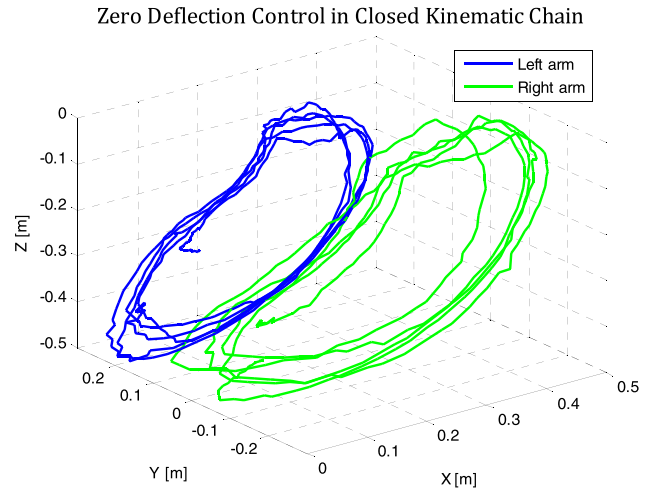

FIGURE 24. Cartesian position of the TCP of both arms when the grasped object is pushed following a circular trajectory in the XZ-plane.
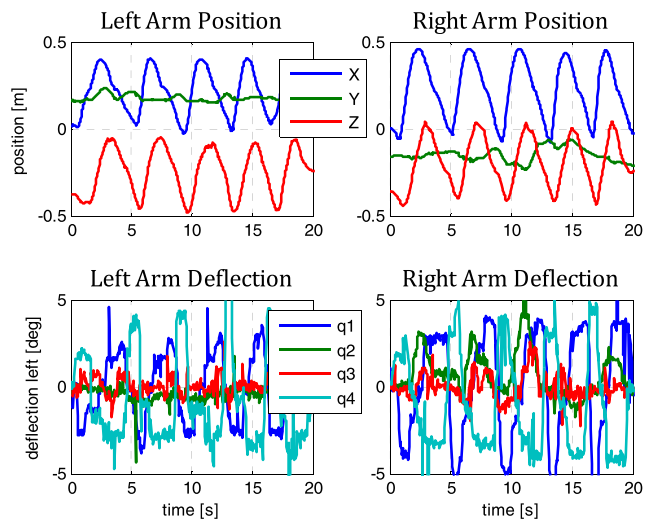

FIGURE 25. TCP position and joint deflection for the circular trajectory.

the tool. The setup and the execution of the experiment are represented in **Fig. 27** and **Fig. 28**.

The UAV was radio-controlled in position by an expert human pilot while an operator took care of the arms from a ground control station (GCS). The tests were conducted in a $6 \times 6 \times 4$ meters area covered by a safety net. The purpose of the developed scenario was illustrating the application of dual arm aerial manipulators to installation and retrieval of inspection tools deployed in areas of difficult access such as high altitude pipes in chemical plants.

The grasping method consisted of guiding the TCP of the left and right arms from their initial position to the grasping points applying the control method shown in **Fig. 7**, closing the grippers when the goal point is reached. The grasping points provided to the arms controller are obtained from the vision algorithm described in [34]. A ZED stereo camera attached to the shoulder structure was employed due to its wide field of view and high image quality. **Fig. 29** shows
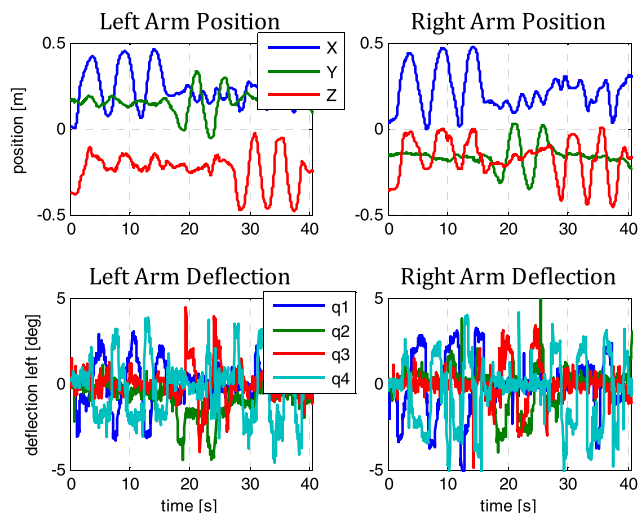
FIGURE 26. Cartesian position of the TCP of left/right arms (up) and joints deflection (down) when the grasped object is pushed along the X (0 – 12 s), Y (15 – 22 s) and Z (22 – 40 s) axes.
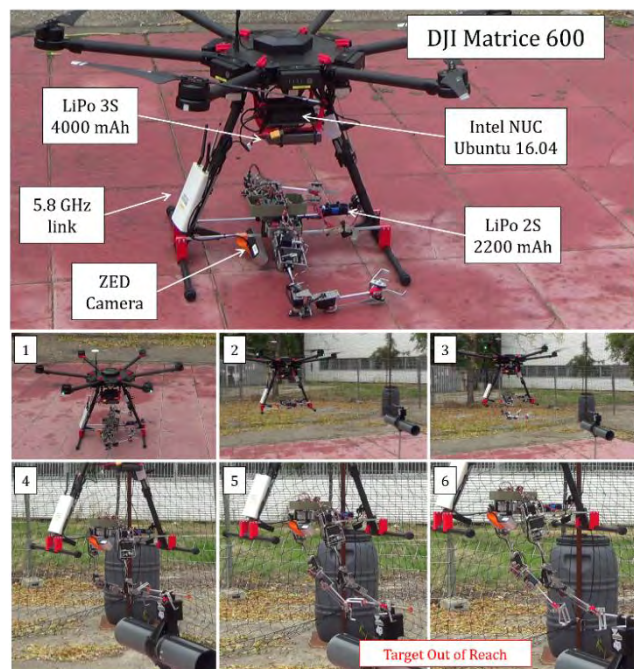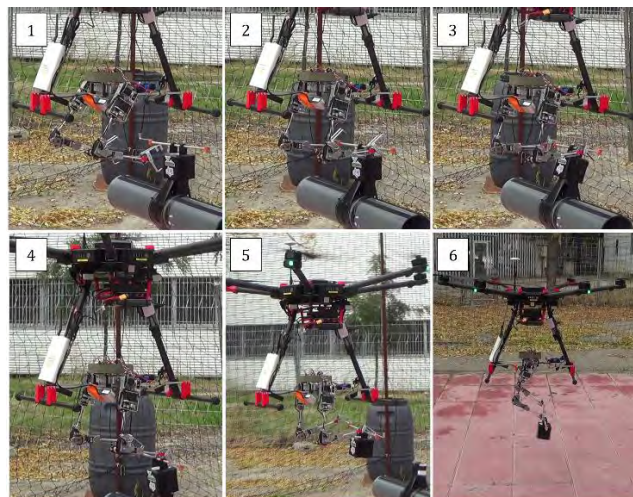

FIGURE 28. Bimanual object grasping on flight. The arms grasp the inspection tool installed over a pipe by a 50 cm length handle.
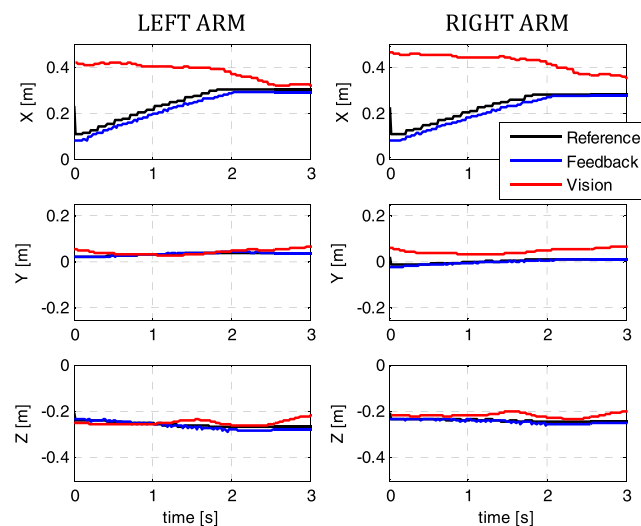

FIGURE 27. Compliant dual arm integrated in DJI Matrice 600 hexarotor. Take-off (1), approaching to inspection tool installed on pipe (2 – 3), and visual servoing (4 – 6). The target points are out of the reach of the arms due to the displacement of the aerial platform (5 – 6).

FIGURE 29. TCP Cartesian position of left/right arms. Grasping points given by the vision (red), reference (black) and servo feedback (blue).

the trajectory of the TCP of left and right arms along with the grasping points given by the vision module during the flight experiment. Positioning errors are mainly due to non-compensated joint deflections and to misalignment errors between the arms frame and the camera frame. The control period and velocity were set to $T = 0.1\ s$, and the reference velocity of the arms was set to $v = 0.2\ m/s$.

The analysis of the video of the outdoor flight tests reveal that the influence of arms motion over the attitude controller in contactless situations is almost negligible, since the mass

and inertia of the manipulator is very low compared to the mass of the multirotor. In [28] we proposed a method for estimating and compensating the reaction torques induced by a stiff-joint dual arm over the base of the aerial platform, identifying separately the gravity, Coriolis, and inertia terms. The torque due to gravity is associated to variations in the position of the end effector, and it is more evident when an object is grasped and lifted, although it is typically cancelled by the integral term of the attitude controller. The effect of the other two dynamic terms can be limited simply adjusting the maximum joint/Cartesian speed of the arms, at expenses of reducing the time performance.

VII. CONCLUSION

This paper detailed the design and mechanical construction of an anthropomorphic, compliant and ultra-lightweight (1.3 kg) dual arm manipulator developed for its integration in a

multi-rotor platform. Both left and right arms provide 4-DOF for end effector positioning in a human-like kinematic configuration. The robust aluminum frame structure and the use of a simple and compact spring-lever transmission mechanism introduced in all the joints provide a high level of protection to the servo actuators against impacts and joint overloads. This features is highly convenient for reducing the cost and time associated to repairs, as the servo actuators represent around the 70% of the cost in materials of the manipulator. One of the main conclusions derived from the experiments is that the capacity of the compliant joints to support impacts and joint overloads associated to motion constraints increases the probability of success in a grasping task with respect to a stiff joint manipulator. The mechanical tolerance of the joints also results extremely useful for the realization of several tasks involving the cooperation of both arms, as bimanual grasping, without requiring a highly accurate coordination of the arms. As future work, it would be necessary to evaluate the accuracy and reliability of the force-torque estimation method.

ACKNOWLEDGMENT

REFERENCES

[1] *AEROARMS Project Home Page*. Accessed: May 5, 2018. [Online]. Available: https://aeroarms-project.eu/

[2] K. Kondak, M. Bernard, N. Meyer, and G. Hommel, "Autonomously flying VTOL-robots: Modeling and control," in *Proc. IEEE Int. Conf. Robot. Autom.*, Apr. 2007, pp. 736–741, doi: 10.1109/ROBOT.2007.363074.

[3] P. E. I. Pounds, D. R. Bersak, and A. M. Dollar, "Grasping from the air: Hovering capture and load stability," in *Proc. IEEE Int. Conf. Robot. Autom.*, May 2011, pp. 2491–2498.

[4] G. Heredia *et al.*, "Control of a multirotor outdoor aerial manipulator," in *Proc. IEEE/RSJ Int. Conf. Intell. Robots Syst.*, Chicago, IL, USA, Sep. 2014, pp. 3417–3422, doi: 10.1109/IROS.2014.6943038.

[5] R. Spica, A. Franchi, G. Oriolo, H. H. Bülthoff, and P. R. Giordano, "Aerial grasping of a moving target with a quadrotor UAV," in *Proc. IEEE/RSJ Int. Conf. Intell. Robots Syst.*, Vilamoura, Portugal, Oct. 2012, pp. 4985–4992, doi: 10.1109/IROS.2012.6385771.

[6] G. Loianno and V. Kumar, "Cooperative transportation using small quadrotors using monocular vision and inertial sensing," *IEEE Robot. Autom. Lett.*, vol. 3, no. 2, pp. 680–687, Apr. 2018, doi: 10.1109/LRA.2017.2778018.

[7] K. Kondak *et al.*, "Aerial manipulation robot composed of an autonomous helicopter and a 7 degrees of freedom industrial manipulator," in *Proc. IEEE Int. Conf. Robot. Autom. (ICRA)*, Hong Kong, May/Jun. 2014, pp. 2107–2112, doi: 10.1109/ICRA.2014.6907148.

[8] S. Kim, S. Choi, and H. J. Kim, "Aerial manipulation using a quadrotor with a two DOF robotic arm," in *Proc. IEEE/RSJ Int. Conf. Intell. Robots Syst.*, Tokyo, Japan, 2013, pp. 4990–4995, doi: 10.1109/IROS.2013.6697077.

[9] A. E. Jimenez-Cano, J. Martin, G. Heredia, A. Ollero, and R. Cano, "Control of an aerial robot with multi-link arm for assembly tasks," in *Proc. IEEE Int. Conf. Robot. Autom.*, Karlsruhe, Germany, May 2013, pp. 4916–4921, doi: 10.1109/ICRA.2013.6631279.

[10] C. D. Bellicoso, L. R. Buonocore, V. Lippiello, and B. Siciliano, "Design, modeling and control of a 5-DoF light-weight robot arm for aerial manipulation," in *Proc. 23rd Medit. Conf. Control Autom. (MED)*, Torremolinos, Spain, Jun. 2015, pp. 853–858, doi: 10.1109/MED.2015.7158852.

[11] R. Cano, C. Pérez, F. Pruaño, A. Ollero, and G. Heredia, "Mechanical design of a 6-DOF aerial manipulator for assembling bar structures using UAVs," in *Proc. 2nd RED-UAS Workshop Res., Edu. Develop. Unmanned Aerial Syst.*, 2013, pp. 1–7.

[12] T. W. Danko and P. Y. Oh, "A hyper-redundant manipulator for mobile manipulating unmanned aerial vehicles," in *Proc. Int. Conf. Unmanned Aircraft Syst. (ICUAS)*, Atlanta, GA, USA, May 2013, pp. 974–981, doi: 10.1109/ICUAS.2013.6564784.

[13] C. Korpela, M. Orsag, and P. Oh, "Towards valve turning using a dual-arm aerial manipulator," in *Proc. IEEE/RSJ Int. Conf. Intell. Robots Syst.*, Chicago, IL, USA, Sep. 2014, pp. 3411–3416, doi: 10.1109/IROS.2014.6943037.

[14] A. Santamaria-Navarro, P. Grosch, V. Lippiello, J. Solà, and J. Andrade-Cetto, "Uncalibrated visual servo for unmanned aerial manipulation," *IEEE/ASME Trans. Mechatronics*, vol. 22, no. 4, pp. 1610–1621, Aug. 2017, doi: 10.1109/TMECH.2017.2682283.

[15] K. Alexis, G. Darivianakis, M. Burri, and R. Siegwart, "Aerial robotic contact-based inspection: Planning and control," *Auto. Robots*, vol. 40, no. 4, pp. 631–655, 2015, doi: 10.1007/s10514-015-9485-5.

[16] J. Thomas, J. Polin, K. Sreenath, and V. Kumar, "Avian-inspired grasping for quadrotor micro UAVs," in *Proc. ASME Int. Design Eng. Tech. Conf. Comput. Inf. Eng.*, 2013, p. 9, doi: 10.1115/DETC2013-13289.

[17] D. Mellinger, Q. Lindsey, M. Shomin, and V. Kumar, "Design, modeling, estimation and control for aerial grasping and manipulation," in *Proc. IEEE/RSJ Int. Conf. Intell. Robots Syst.*, San Francisco, CA, USA, Sep. 2011, pp. 2668–2673, doi: 10.1109/IROS.2011.6094871.

[18] T. Bartelds, A. Capra, S. Hamaza, S. Stramigioli, and M. Fumagalli, "Compliant aerial manipulators: Toward a new generation of aerial robotic workers," *IEEE Robot. Autom. Lett.*, vol. 1, no. 1, pp. 477–483, Jan. 2016, doi: 10.1109/LRA.2016.2519948.

[19] M. Fumagalli *et al.*, "Developing an aerial manipulator prototype: Physical interaction with the environment," *IEEE Robot. Autom. Mag.*, vol. 21, no. 3, pp. 41–50, Sep. 2014.

[20] B. Yüksel, S. Mahboubi, C. Secchi, H. H. Bülthoff, and A. Franchi, "Design, identification and experimental testing of a light-weight flexible-joint arm for aerial physical interaction," in *Proc. IEEE Int. Conf. Robot. Autom. (ICRA)*, Seattle, WA, USA, May 2015, pp. 870–876, doi: 10.1109/ICRA.2015.7139280.

[21] D. W. Robinson, J. E. Pratt, D. J. Paluska, and G. A. Pratt, "Series elastic actuator development for a biomimetic walking robot," in *Proc. IEEE/ASME Int. Conf. Adv. Intell. Mechatronics*, Atlanta, GA, USA, Sep. 1999, pp. 561–568, doi: 10.1109/AIM.1999.803231.

[22] J. Pratt, B. Krupp, and C. Morse, "Series elastic actuators for high fidelity force control," *Ind. Robot., Int. J.*, vol. 29, no. 3, pp. 234–241, 2002.

[23] S. Oh and K. Kong, "High-precision robust force control of a series elastic actuator," *IEEE/ASME Trans. Mechatronics*, vol. 22, no. 1, pp. 71–80, Feb. 2017, doi: 10.1109/TMECH.2016.2614503.

[24] H. Vallery, R. Ekkelenkamp, H. van der Kooij, and M. Buss, "Passive and accurate torque control of series elastic actuators," in *Proc. IEEE/RSJ Int. Conf. Intell. Robots Syst.*, San Diego, CA, USA, Oct./Nov. 2007, pp. 3534–3538, doi: 10.1109/IROS.2007.4399172.

[25] A. Suarez, G. Heredia, and A. Ollero, "Lightweight compliant arm for aerial manipulation," in *Proc. IEEE/RSJ Int. Conf. Intell. Robot Syst. (IROS)*, Hamburg, Germany, Sep./Oct. 2015, pp. 1627–1632, doi: 10.1109/IROS.2015.7353585.

[26] A. Suarez, G. Heredia, and A. Ollero, "Lightweight compliant arm with compliant finger for aerial manipulation and inspection," in *Proc. IEEE/RSJ Int. Conf. Intell. Robot Syst. (IROS)*, Daejeon, South Korea, Oct. 2016, pp. 4449–4454, doi: 10.1109/IROS.2016.7759655.

[27] *ProDrone Aerial Manipulator Web Page*. Accessed: May 5, 2018. [Online]. Available: https://www.prodrone.jp/en/ concept/pd6b-aw-arm/

[28] A. Suarez, A. E. Jimenez-Cano, V. M. Vega, G. Heredia, A. Rodríguez-Castaño, and A. Ollero, "Lightweight and human-size dual arm aerial manipulator," in *Proc. Int. Conf. Unmanned Aircraft Syst. (ICUAS)*, Miami, FL, USA, Jun. 2017, pp. 1778–1784, doi: 10.1109/ICUAS.2017.7991357.

[29] L. Zhou and S. Bai, "A new approach to design of a lightweight anthropomorphic arm for service applications," *J. Mech. Robot.*, vol. 7, no. 3, p. 031001, 2015, doi: 10.1115/1.4028292.

[30] C. Ott, A. Albu-Schäffer, A. Kugi, and G. Hirzinger, "On the passivity-based impedance control of flexible joint robots," *IEEE Trans. Robot.*, vol. 24, no. 2, pp. 416–429, Apr. 2008.

[31] L. Yan, Z. Mu, W. Xu, and B. Yang, "Coordinated compliance control of dual-arm robot for payload manipulation: Master-slave and shared force control," in *Proc. IEEE/RSJ Int. Conf. Intell. Robots Syst. (IROS)*, Oct. 2016, pp. 2697–2702.

[32] E. Papadopoulos and S. A. A. Moosavian, "Dynamics and control of space free-flyers with multiple manipulators," *Adv. Robot.*, vol. 9, no. 6, pp. 603–624, 1994.

[33] E. Simetti and G. Casalino, "Whole body control of a dual arm underwater vehicle manipulator system," *Annu. Rev. Control*, vol. 40, pp. 191–200, Jan. 2015.

[34] P. R. Soria, B. C. Arrue, and A. Ollero, "Detection, location and grasping objects using a stereo sensor on UAV in outdoor environments," *Sensors*, vol. 17, no. 1, p. 103, 2017.

GUILLERMO HEREDIA was Visiting Researcher with the Field Robotics Centre, Carnegie Mellon University, Pittsburgh, PA, USA, and worked for an International Automobile Manufacturer (General Motors). He participated as a senior researcher in 50 Research and Development projects (EU, NASA, and national projects) leading 10 of them, including the Spanish team of the FP7-EC project ECSAFEMOBIL and the AERO-CROS national project. He is currently a Professor with the University of Seville, Spain. He is author or co-author of over 70 publications on aerial manipulation, autonomous vehicles, and fault detection and reconfiguration. He is currently member of the Board of Directors of the Spanish Robotics Research and Development Society SEIDROB.

ALEJANDRO SUAREZ received the degree in telecommunication engineering and the M.Sc. degree in automation and robotics from the University of Seville, Spain, in 2012 and 2013, respectively. Since 2012, he has been with the Robotics, Vision and Control Group, University of Seville, involved in the FP7 EC-SAFEMOBIL project, and in the PERIGEO and CLEAR Spanish projects. In 2014, he received a FPU Grant from the Spanish Ministry of Education, Culture and Sport for supporting his research activity as Ph.D. student in the frame of the AEROARMS H2020 project. He stayed three months at the Robotics and Mechatronics Institute, DLR, Oberpfaffenhofen. His research interests are humanoid robotics and the design and development of anthropomorphic, and compliant and lightweight robotic arms intended to aerial manipulation.

ANIBAL OLLERO has been a Full Professor with the Universities of Santiago and Malaga (Spain), Researcher with the Robotics Institute, Carnegie Mellon University, Pittsburgh, PA, USA, and LAAS-CNRS, Toulouse, France. He is currently a Full Professor and a Head of GRVC, University of Seville, and a Scientific Advisor of the Center for Advanced Aerospace Technologies, Seville, Spain. He authored over 650 publications, including 10 books and 130 journal papers and led about 150 projects, transferring results to many companies. He has participated in 25 European Projects being coordinator of six, including the current ERC Advanced Grant GRIFFIN and the H2020 AEROARMS. He was a recipient of 15 awards, has supervised 36 Ph.D. Thesis, and is currently a co-chair of the IEEE Technical Committee on Aerial Robotics and Unmanned Aerial Vehicles and a member of the Board of Directors and coordinator of the Aerial Robotics Topic Group of euRobotics.

● ● ●